

Mechanical properties of a novel fiber-bridging interface for connecting FRP profile and concrete

Hongwei Lin^{a,b}, Haidong Qu^a, Peng Feng^{c,*}, Huixin Zeng^a, Guanzhi Cheng^d

^a School of Civil Engineering, Beijing Jiaotong University, Beijing 100044, China

^b Key Laboratory of Concrete and Prestressed Concrete Structures of Ministry of Education, Southeast University, Nanjing 210096, China

^c Department of Civil Engineering, Tsinghua University, Beijing 100084, China

^d Railway Engineering Research Institute, China Academy of Railway Sciences Co., Ltd., Beijing 100081, China

ARTICLE INFO

Keywords:

FRP
Concrete
Interface
Bond stress-slip
Finite element
Machine learning

ABSTRACT

The connection between FRP profile and concrete is critical for structural performance. This study introduces a novel fiber-bridging interface to enhance the FRP-concrete interfacial behavior. The interface comprises an epoxy resin adhesive layer, a carbon fabric layer, a mixture of adhesive and sand layer, and U-shaped steel fibers. Central pull-out tests were conducted to investigate the mechanical performance of this novel interface. The investigated variables included bond length and fiber volume fraction. Test results indicate that all specimens failed in a brittle mode at the adhesive layer, with load plateauing after reaching the peak. The number of steel fibers had limited influence on the interfacial behavior. Based on the load-slip curves, a bond stress-slip model for the tangential behavior was developed. An interfacial expansion model was further developed by means of FE analysis and machine learning. The three most widely used machine learning models, i.e., the BP neural network model, the random forest model, and the XGBoost model were selected. Comparisons show that all three models provide reasonable predictions, with the XGBoost model demonstrating the best performance. These models for the tangential and normal behavior of FRP-concrete interface were implemented into FE models for numerical analysis. Comparisons between numerical and experimental results show that the proposed models accurately describe the interfacial behavior of the fiber-bridging interface under brittle failure mode. The innovative interface proposed in this paper can be used for connecting concrete and FRP in various scenarios, and the proposed methodology of calibrating local bond behavior parameters from global response offers a new approach for establishing interfacial bond models.

1. Introduction

Corrosion of reinforced concrete structures in aggressive environments is a significant global issue. Annually, substantial economic losses due to steel corrosion are caused [1]. The application of fiber reinforced polymer (FRP) in engineering structures offers a promising solution to this problem. FRP materials are lightweight, possess high strength, and are resistant to corrosion, making them ideal for use in corrosive environments [2–4]. Combining FRP and concrete can fully exploit the material merits of both materials, leading to the development of durable and lightweight structures [5]. To gain excellent mechanical performance of FRP-concrete hybrid structures, it is of paramount importance to ensure FRP and concrete work together effectively under external forces. This therefore requires an effective connection between FRP and

concrete interface. However, the surface of pultruded FRP profiles is typically very smooth, posing a challenge for effective bonding with concrete. Various interfacial configurations have been proposed to improve the FRP profile-concrete interface, including wet-bonding interface, sand-coating interface, bolt connections, perforation connections, and shear-key connections, among others.

The wet-bonding interface is constructed by coating the surface of FRP profiles with adhesive and then pouring concrete before the adhesive layer fully hardens. It allows the concrete and adhesive layer to cure simultaneously [6–10]. Existing studies indicate that the failure mode of wet-bonding interface is similar to the dry-bonding interface. Based on the bond models of dry-bonding interface, Wang et al. [8,11] and Zhang et al. [6,7] established bond stress-slip models for wet-bonding interface. The study by the authors found that the interfacial behavior of

* Corresponding author.

E-mail address: fengpeng@tsinghua.edu.cn (P. Feng).

<https://doi.org/10.1016/j.engstruct.2024.119320>

Received 28 March 2024; Received in revised form 4 August 2024; Accepted 14 November 2024

Available online 23 November 2024

0141-0296/© 2024 Elsevier Ltd. All rights reserved, including those for text and data mining, AI training, and similar technologies.

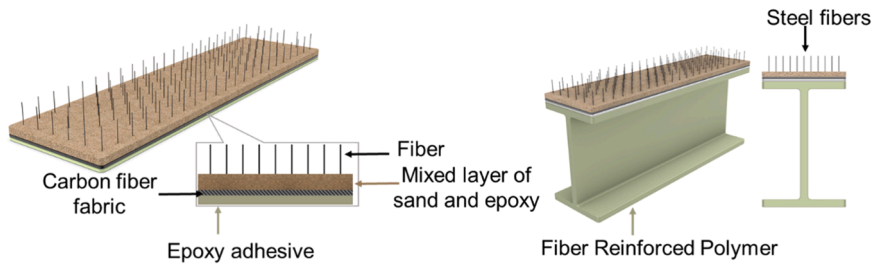


Fig. 1. Schematic illustration of the newly developed fiber-bridging interface.

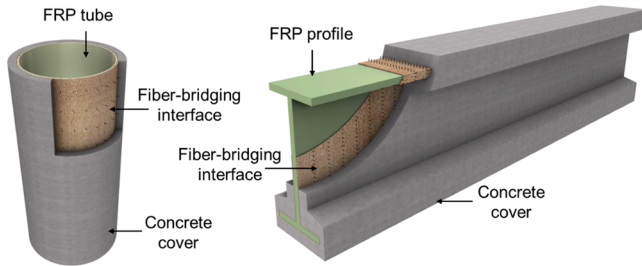


Fig. 2. Application of the novel interface in concrete-encased FRP tube / FRP profile.

wet-bonding interface could be significantly improved by the lateral confinement [12].

The sanding-coating interface is constructed by applying adhesive to the surface of FRP profiles and then adhering gravel before the adhesive layer hardens. This method provides good interfacial shear strength and stiffness but relatively low bonding strength in the normal direction. Some researchers [13–20] have studied the influence of various parameters on the interfacial behavior of sand-coating interface. For sand-coating interface with lateral confinement, a pressure-dependent bond model was proposed by the authors [21].

Compared with the above two interfaces, bolt connections exhibit higher interfacial resistance and better interfacial ductility [22–29]. Hai et al. [26] found that inclined steel bolts could increase the deformation capacity of the bolted interface. FRP bolts have also been applied for FRP-concrete interface. According to Honickman et al. [30] and Xue et al. [27], FRP bolts had lower interfacial load-bearing capacity and stiffness compared to steel bolts and were prone to brittle failure. The disadvantage with bolt connections is that the interfacial stiffness is relatively low, resulting in unfavorable deformation of FRP-concrete structures [31,32]. To address this issue, researchers proposed the combined use of sand-coating or wet bonding interfaces with bolt connections to form hybrid interface [26,33–36]. However, the failure of

sand-coating or wet-bonding interface occurs before the bolts, so the load-bearing capacity of bolts can only be considered as a strength reserve.

For hybrid FRP-concrete beams and slabs, perforation of FRP profiles is also a commonly adopted interfacial connection. Perforation connection creates holes on the profiles, allowing concrete to flow in and form dowels. To further improve the interfacial behavior, steel or FRP bars penetrating the holes can be used as reinforcement. This method is similar to the PBL (perforated rib in English or perfobond leist in German) connectors for steel-concrete composite structures [37–39]. There are two common perforation connections: perforation on the flanges of FRP profiles [37,40,41] and perforation on the webs or ribs of FRP profiles [42–46]. The failure mode of perforation interface tends to be shear failure of FRP profile [44,47]. Some researchers have also studied the performance of shear-key connections [7,48].

In summary, existing interfacial connections all have limitations. Interfaces with satisfying interfacial strength, stiffness and ductility are still in high demand. In view of this, this paper proposes a novel FRP-concrete interface, i.e., the fiber-bridging interface, which can result in favorable interfacial behavior in both the tangential and normal direction. As shown in Fig. 1, this interface consists of four parts: an epoxy resin adhesive layer, a carbon fabric layer, a mixture of adhesive and sand layer, and U-shaped steel or synthetic fibers anchored by the carbon fiber fabric layer. Compared with the existing interfaces, this new interface offers several advantages: (1) the mechanical interlock between fibers, sand and concrete can provide favorable interfacial strength in both tangential and normal directions; (2) the interfacial pressure due to fiber-tension can contribute to frictional resistance in the tangential direction; (3) a ductile interfacial behavior can be achieved by means of the deformation of fibers and the slip between fibers and concrete. By adjusting the number of fibers or the fiber volume fraction, different interfacial behavior can be obtained.

The potential applications of this novel interface include hybrid FRP profile-concrete beam, concrete-encased FRP tube (Fig. 2a) and FRP profile (Fig. 2b). In FRP-concrete hybrid beam, the novel interface can

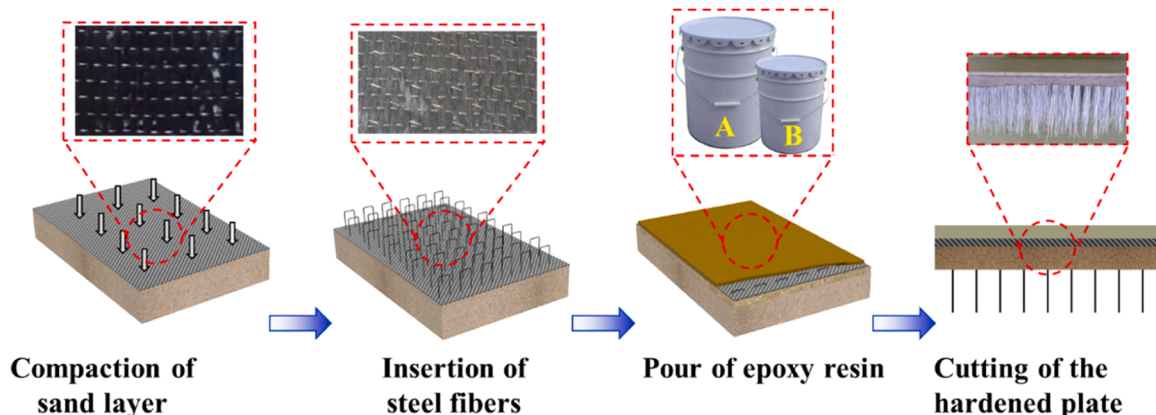


Fig. 3. Schematic illustration of fabricating the fiber-bridging interface.

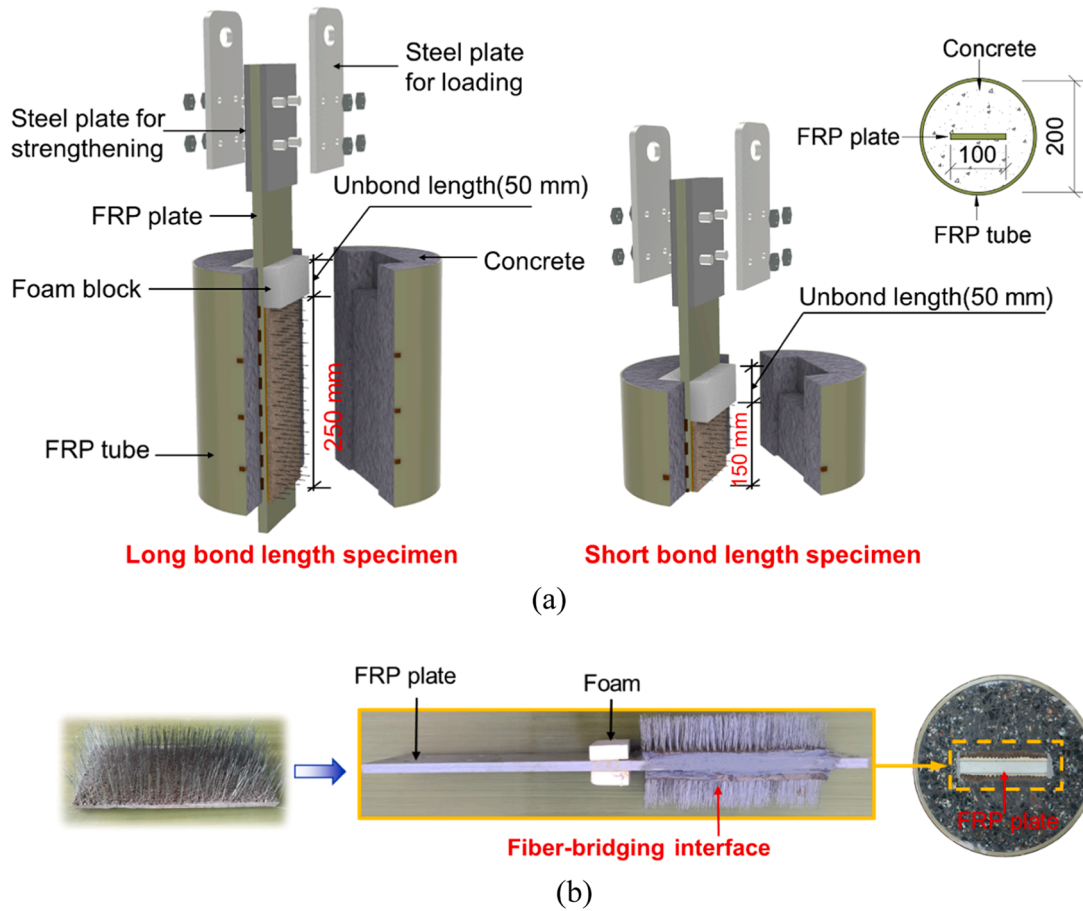


Fig. 4. Configuration of the pullout specimens: (a) specimen geometry; (b) fiber-bridging interface.

Table 1
Details of the tested specimens.

Designation	Height (mm)	Bond length (mm)	Fiber volume fraction (η)	Bond Areas (mm ²)	Strain gauges
L-V1 -1	300	250	1.5 %	100 mm × 250 mm	7 strain gauges on FRP plate and 8 strain gauges on FRP tube
L-V1 -2	300	250			no strain gauges
S-V1 -3	200	150		100 mm × 150 mm	8 strain gauges on FRP tube
L-V2 -1	300	250	3.0 %	100 mm × 250 mm	no strain gauges
L-V2 -2	300	250			no strain gauges
S-V2 -3	200	150		100 mm × 150 mm	8 strain gauges on FRP tube

Note: for the specimen label, “L” means long bond length, “S” means short bond length, “V1” means fiber volume fraction $\eta = 1.5\%$, “V2” means $\eta = 3.0\%$; “1, 2, and 3” means the serial number in the group of specimens with the same fiber volume fraction.

Table 2
Concrete mixture proportions (kg/m³).

Water	Cement	Fine aggregates	Coarse aggregates	Water reducing admixture
204	408	583	962	1.2

provide significant shear strength in the tangential direction and anchorage strength in the normal direction, preventing the debonding or the lift of the concrete slab. In concrete-encased FRP tube and FRP profile, the novel interface can effectively prevent the spalling of concrete cover, hereby increasing the durability, fiber resistance, and local bearing capacity of FRP tube and profile.

The behavior of fiber-bridging interface is governed by several parameters to be investigated. Therefore, the aims of this paper are to reveal the behavior of the novel interface with high fiber volume fractions and develop bond models for analysis. Central pullout tests are conducted, and the failure modes are analyzed. Based on experimental results, FE simulation and machine learning algorithms, bond models for this novel interface are established. The results in this paper can serve as a reference for optimizing the parameters of the fiber-bridging interface.

2. Experimental program

2.1. Fabrication of the fiber-bridging interface

The fiber-bridging interface was composed of a CFRP sheet, steel fibers, permeable epoxy resin adhesive, and fine river sand. The CFRP sheet had a tensile strength of 3400 MPa and an elastic modulus of 230 GPa. The steel fibers, made of Q195 steel, had a diameter of 0.4 mm

Table 3
Mechanical properties of the FRP plate.

Longitudinal direction			Young's modulus (GPa)		Transverse direction	
Strength (MPa)					Compressive	
Tensile	Compressive	In-plane shear	Tensile	Compressive	Strength (MPa)	Young's modulus (GPa)
531	377	32.3	33.2	24.0	108.3	11.2

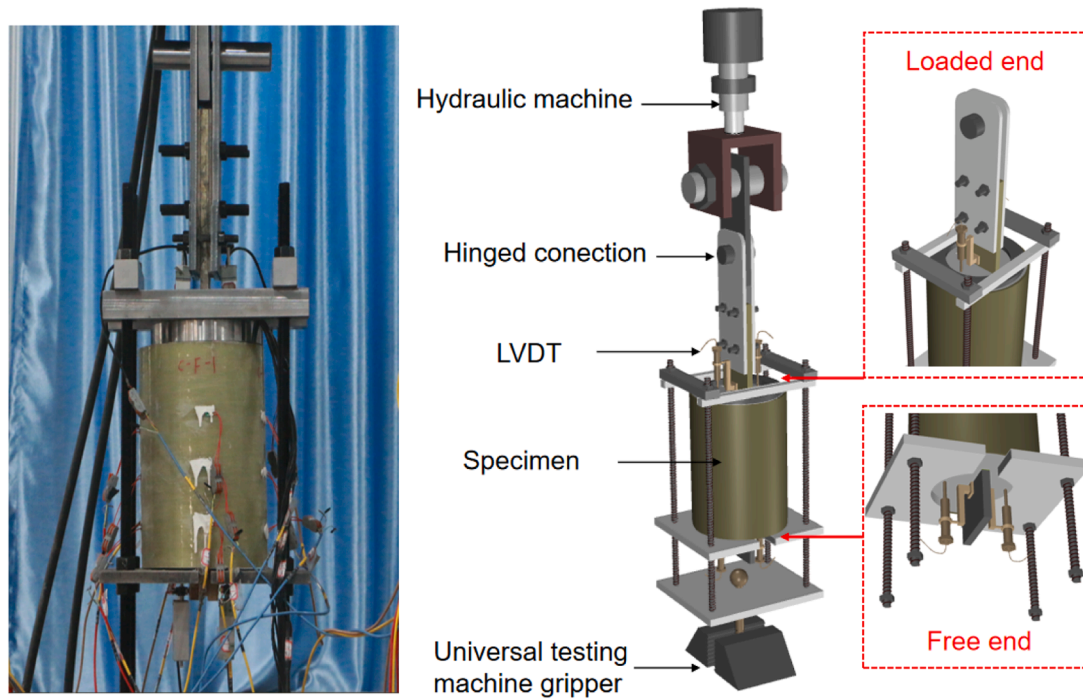


Fig. 5. Test setup of specimens.

2.2. Test specimen

In many scenarios, the FRP-concrete interface is subjected to lateral confinement [49–51]. To simulate the stress conditions of an interface with lateral confinement, this study designed six central pull-out specimens (see Fig. 4a). These specimens were composed of an FRP tube, a confined concrete block, and a centrally positioned FRP plate. The fiber-bridging interface is used to connect the FRP plate and concrete. The FRP tube had a diameter of 200 mm and a wall thickness of 4.5 mm. The FRP plate had a cross-section of 101.6 mm × 12.7 mm. An unbond zone was created within the 50 mm-length from the loaded end using foam blocks. In the bond zone, the surface of the FRP plate was first roughened by coarse sandpaper and then cleaned with industrial alcohol. After that, the fiber-bridging interfaces in the form of pre-fabricated plates were bonded to the FRP plate using structural adhesive (see Fig. 4b).

The two most important parameters influencing the behavior of the fiber-bridging interface, i.e., the bond length and the number of steel fibers are selected as variables. Two bond lengths, i.e., 250 mm and 150 mm, were examined. Defining the ratio of the cross-sectional area of steel fibers to the bonded area as the fiber volume fraction (η), two fiber volume fractions, namely $\eta = 1.5\%$ and $\eta = 3.0\%$, were adopted. It should be noted that the values for each parameter were tentatively set in order to obtain the full range of interfacial behavior and different failure modes. The dimensions of the prefabricated fiber-bridging interface slabs were 100 mm × 250 mm and 100 mm × 150 mm for long and short bond length specimens, respectively. The thickness of the interface was approximately 5 mm, and the exposed fiber length was

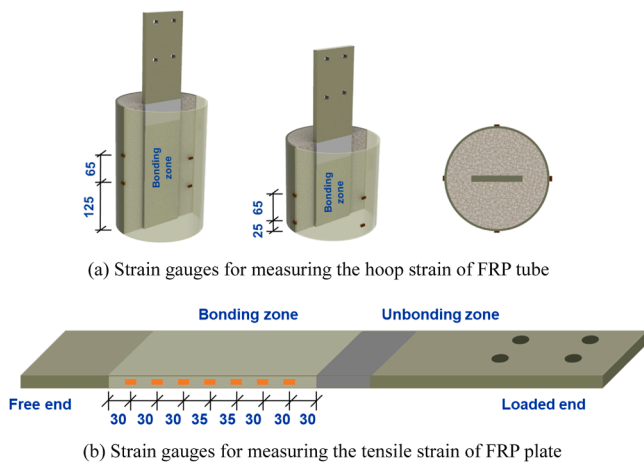


Fig. 6. Locations of strain gauges.

and were bent into a U-shape. The manufacture of the fiber-bridging interface is illustrated in Fig. 3. First, the CFRP sheet was laid on top of the compacted sand layer, then the U-shaped fibers were threaded through the CFRP sheet and inserted into the sand layer. Finally, a highly flowable epoxy resin adhesive was poured onto the CFRP sheet. The epoxy resin adhesive gradually infiltrated the sand layer and eventually hardened. By removing the sand that was not bonded by adhesive, the fiber-bridging interfaces in the form of precast slabs were obtained.

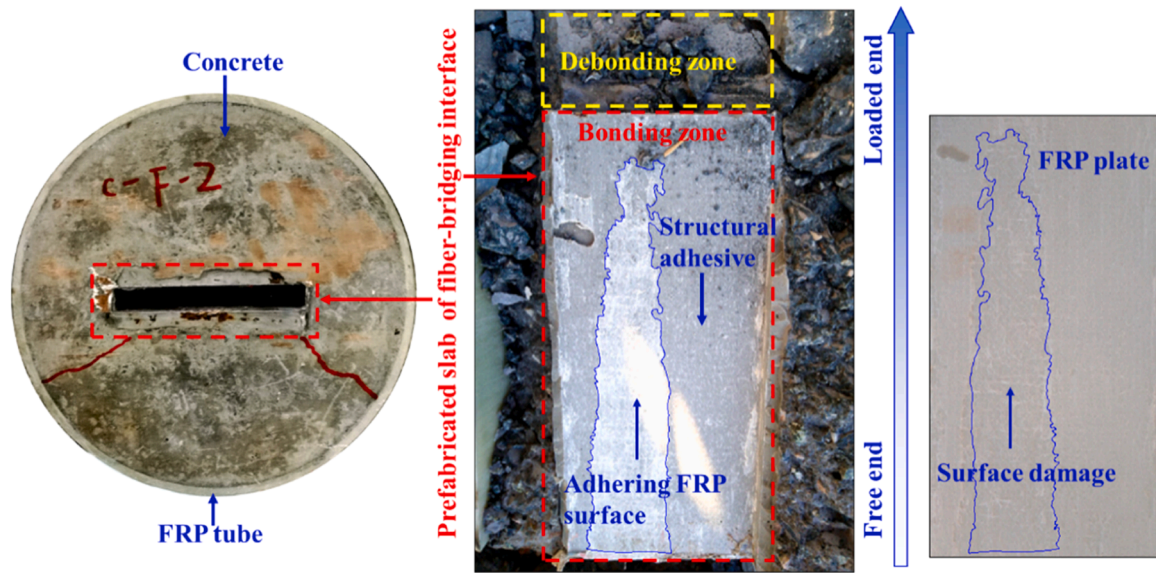


Fig. 7. The failure mode of specimen L-V1-2.

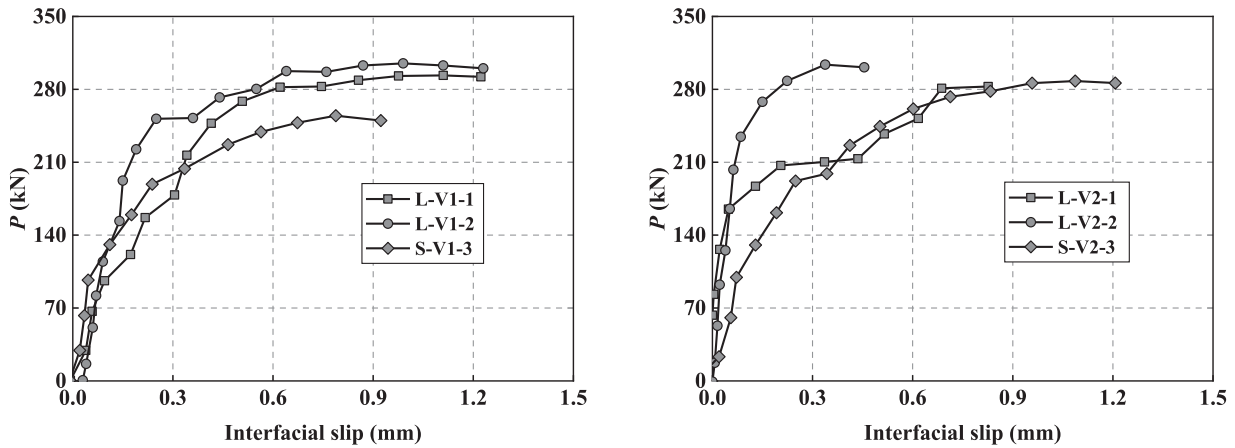


Fig. 8. Load-loaded end slip curves.

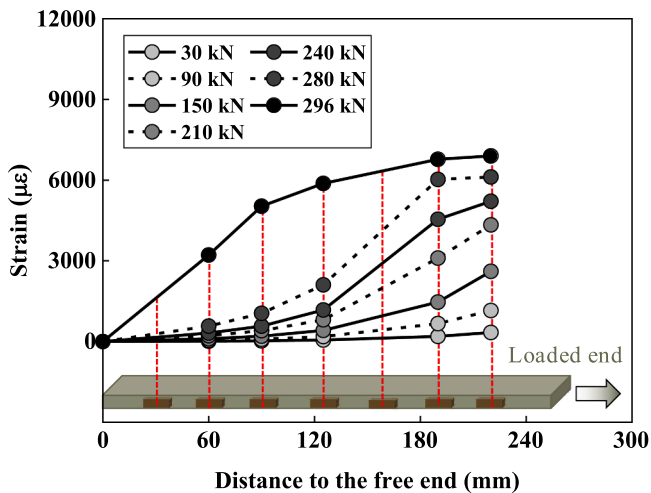


Fig. 9. The distribution of the tensile strain of FRP plate.

about 40 mm. Details of all the specimens are listed in Table 1.

2.3. Material properties

2.3.1. Concrete

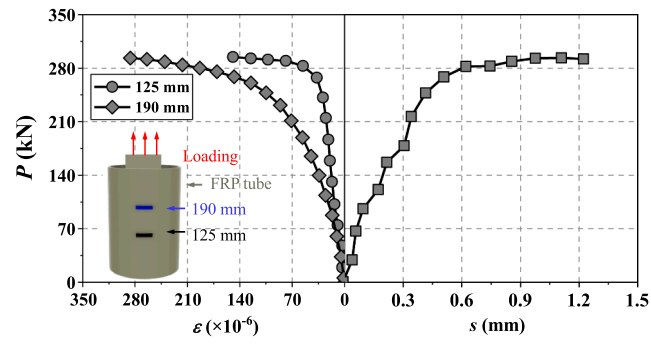
C40 concrete was used for specimen fabrication, and its mixture proportion is shown in Table 2. At the time of loading tests, the tested compressive strength on cubes (150 mm × 150 mm × 150 mm) was 45.7 MPa, and on prisms (150 mm × 150 mm × 300 mm) was 32.7 MPa.

2.3.2. FRP tube

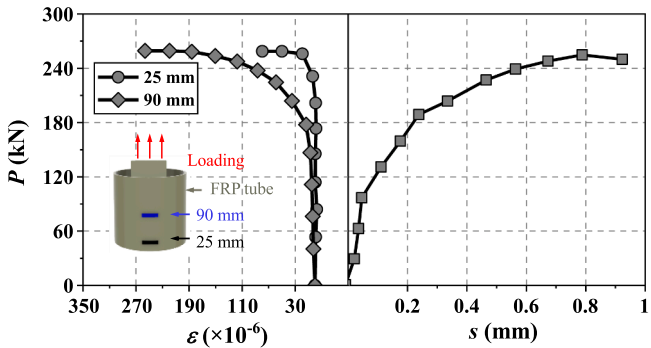
The FRP tube was made of E-glass fibers and epoxy resin using filament-winding technique. E-glass fibers, a type of fiberglass initially developed for electrical applications, are commonly used in reinforced plastics due to their excellent mechanical properties and insulating properties. The fiber volume fraction was 75 %, and the fiber orientation was ± 85° with respect to the longitudinal axis. According to the manufacturer, the longitudinal and hoop tensile strengths were 41 MPa and 695 MPa, respectively. The hoop elastic modulus was 32.7 GPa.

2.3.3. FRP plate

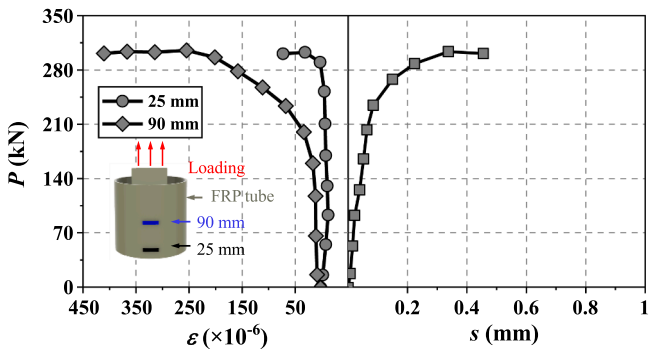
The FRP plates were made of E-glass fibers and polyethylene resin



(a) L-V1-1



(b) S-V1-3



(c) S-V2-3

Fig. 10. Development of hoop strain of FRP tube.

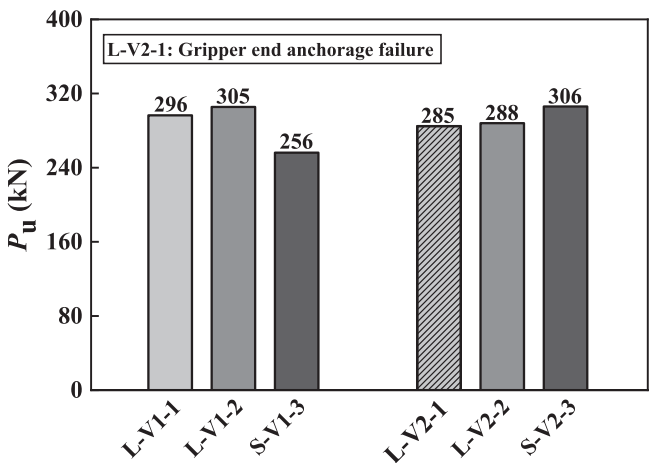


Fig. 11. The ultimate load P_u of all specimens.

matrix, and manufactured through pultrusion technology. The mechanical properties of the FRP plate are listed in Table 3. To prevent potential FRP material failure at the clamping end, both sides of the plate were strengthened by two 6 mm-thick steel plates, each with a length of 180 mm.

2.3.4. Adhesive

The structural adhesive used for bonding the fiber-bridging interface was a two-component modified construction epoxy adhesive. The tested tensile strength and elastic modulus of the adhesive were 45 MPa and 7.2 GPa, respectively.

2.4. Test setup and instrumentation

Fig. 5 shows the specimen under the loading test. The specimen was fixed on an assembled reaction frame, and the FRP plate was gradually pulled out of the concrete with a constant rate of 0.4 mm/min. To monitor the slip at the interface, two linear variable displacement transformers (LVDTs) were installed at the loaded end and the free end, respectively.

Fig. 6(a) shows the locations of the strain gauges in the hoop direction. For the long bond length specimens, 4 strain gauges were uniformly attached along the circumferential direction at heights of 125 mm and 190 mm. For the short bond length specimens, 4 strain gauges were arranged at heights of 25 mm and 65 mm. To measure the tensile strain of FRP plate of the long bond length specimen, 7 strain gauges were attached at different locations from the loaded end to the free end, as shown in Fig. 6(b). During the loading, all test data were automatically collected by a computer-aided data acquisition system.

3. Experimental results

3.1. Failure modes

Only specimen L-V2-1 failed at the clamping end. The FRP plate failed in a shear-out failure mode. All other specimens failed in a brittle manner at the adhesive layer, as illustrated in Fig. 7. After detachment from the FRP plate, the prefabricated slab was left in the concrete. Clear surface damage on the FRP plate was observed, with parts of the surface mat peeling off. The brittle failure of the novel interface is attributed to the very high fiber volume fraction. The interfacial resistance of the steel fibers surpassed that of the adhesive layer. A parallel study based on single-lap shear tests by the authors demonstrates that a fiber volume fraction of 0.4 % results in a ductile failure of the novel interface.

3.2. Load-slip relationships

Fig. 8 presents the load-slip curves at the loaded end. The load-slip curves include three stages: the linear ascending stage, the curved ascending stage, and the plateau stage. When the load reaches the peak, it plateaus, indicating a progressive debonding failure. Compared with the short bond length specimens, long bond length specimens exhibit a longer plateau stage.

3.3. Strains of FRP plate and FRP tube

Fig. 9 shows the tensile strains of FRP plate of specimen L-V1-1. From the loaded end to the free end, the tensile strain gradually decreases. Initially, only parts of the FRP plate exhibit noticeable tensile strain, and the tensile strain near the free end is minimal. As the load approaches the peak, the strain gradient near the loaded end decreases to zero. This indicates that the interface at the loaded end is completely damaged and the load transfer has failed.

Fig. 10 shows the measured hoop strains of the FRP tube. Significant hoop strain was generated, indicating the expansion of concrete matrix. This is because any tangential sliding between two microscopically

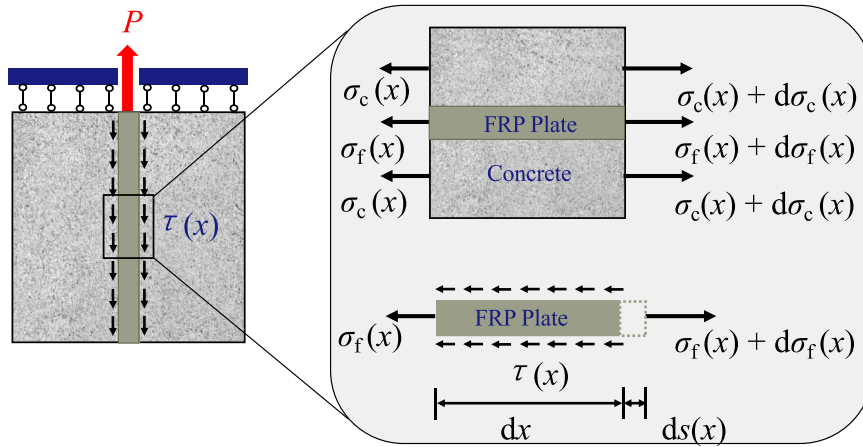
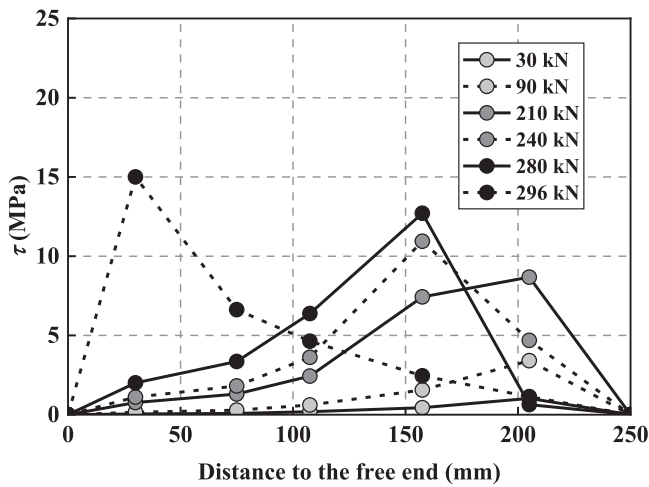


Fig. 12. Stress state of FRP-concrete interface.



(a)

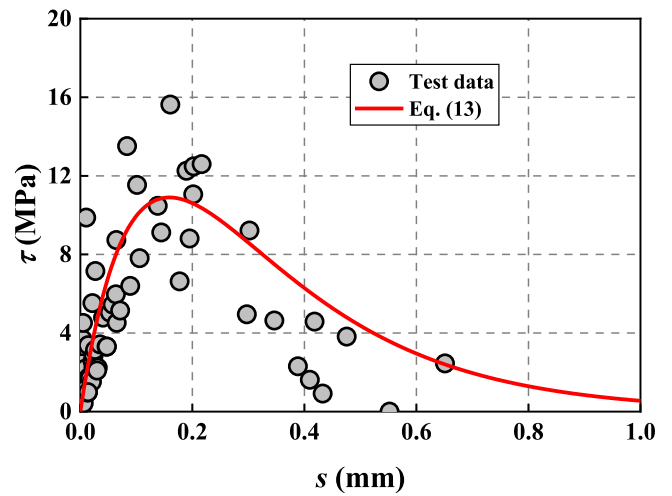
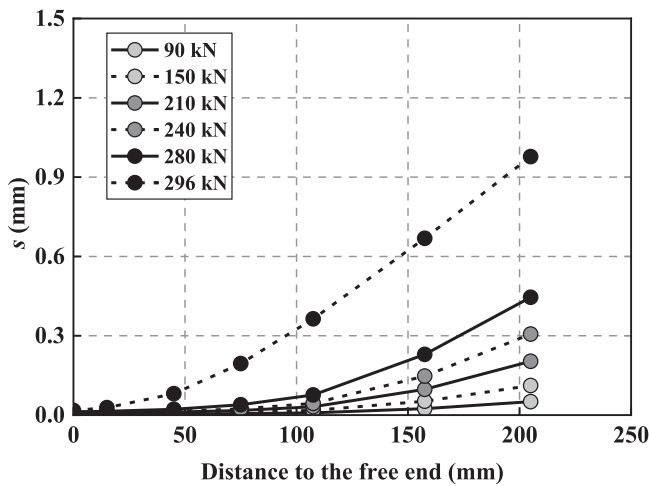


Fig. 14. Interfacial stress versus slip curves.



(b)

Fig. 13. The calculated bond stress (a) and slips (b) at different locations of specimen L-V1-1.

surfaces will generally also entail a lateral displacement [52]. In the early stages of loading, the interface is hardly damaged, and hoop strains increase slowly. At the peak, debonding failure occurs at the interface,

inducing apparent interfacial expansion and consequent hoop strains in the FRP tube.

4. Analysis and discussions

4.1. Ultimate load

Fig. 11 shows the ultimate loads of specimens. The ultimate loads of the specimens with different fiber volume fraction are very close. This is because all the specimens failed at the surface of FRP plate, and the parameters of the fiber-bridging interface show limited influence. Additionally, it can be noted that the ultimate loads of specimens with shorter bond lengths are close to those of specimens with longer bond length. According to previous research [53–58], there exists an effective bond length for brittle interfaces. Beyond the effective bond length, the ultimate load of the interface no longer increases, and the load remains constant after reaching the peak. Based on Figs. 7 to 11, it can be inferred that the bond length of 250 mm exceeds the effective bond length.

4.2. Bond stress

Based on the equilibrium conditions of FRP plate (Fig. 12), the following equation can be obtained,

$$A_f \sigma_f + \tau dx b_f = A_f (\sigma_f + d\sigma_f) \quad (1)$$

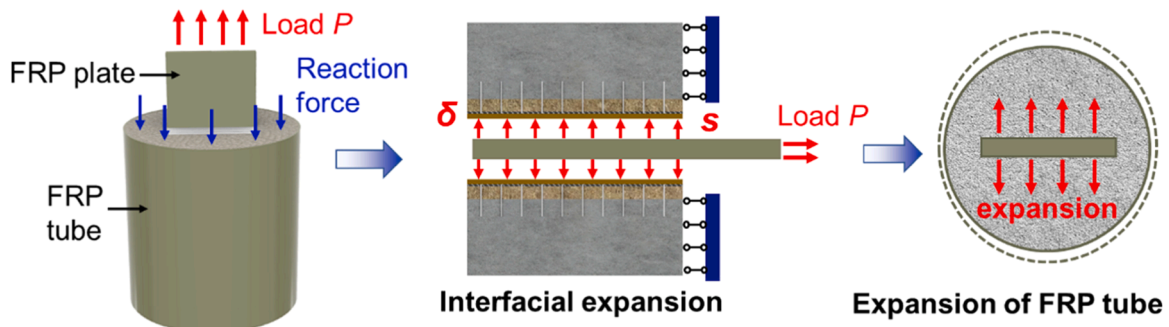


Fig. 15. Schematic illustration of shear-expansion effect of FRP-concrete interface.

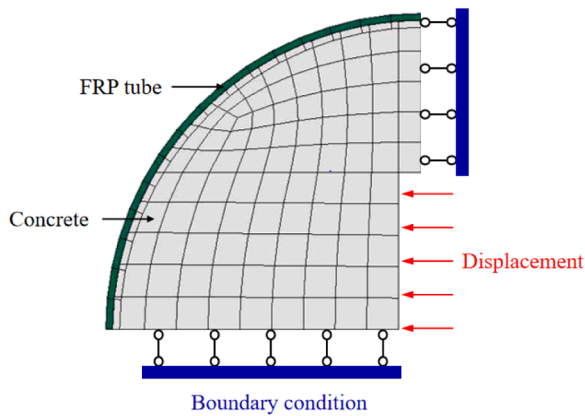


Fig. 16. FE model for the simulation of interfacial dilatation.

where σ_f is tensile stress; A_f is the cross-section area, $A_f = t_f \times b_f$, t_f and b_f are respectively the thickness and width of FRP plate. Eq. (1) can be transformed into the following equation:

$$\frac{d\sigma_f(x)}{dx} - \frac{\tau(x)}{t_f} = 0 \quad (2)$$

The stress-strain relationship is,

$$\sigma_f(x) = E_f \varepsilon_f(x) \quad (3)$$

where E_f is the elastic modulus. Substituting Eq. (3) into Eq. (2),

$$\tau(x) = \frac{d\varepsilon_f(x)}{dx} E_f t_f \quad (4)$$

Converting Eq. (4) into a difference equation,

$$\tau_{i+1,i} = \frac{t_f E_f (\varepsilon_{i+1} - \varepsilon_i)}{\Delta x_{i+1,i}} \quad (5)$$

where $\tau_{i+1,i}$ is the average bond stress between positions x_{i+1} and x_i ; ε_{i+1} and ε_i are the strain values obtained from strain gauges.

Fig. 13(a) shows the bond stress of specimen L-V1-1 based on Eq. (5). In the early stages of loading, the peak bond stress appears near the loaded end. As the load increases, the peak of bond stress moves towards the free end. When the load reaches its peak, the peak of bond stress is near the free end, while the bond stress near the loaded end is close to zero, indicating debonding failure at the loaded end. A similar phenomenon has been reported by previous studies [58].

4.3. Interfacial slip

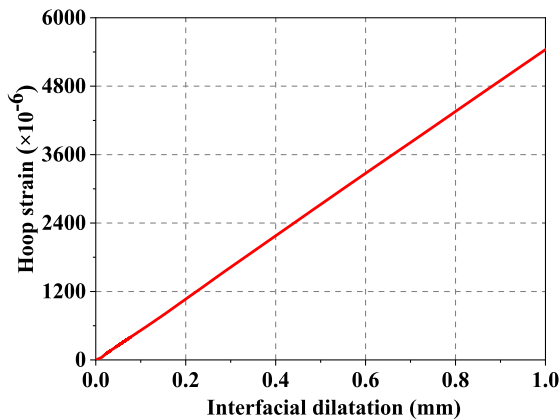
According to the deformation compatibility conditions at the interface,

$$s = \int (\varepsilon_f - \varepsilon_c) dx \quad (6)$$

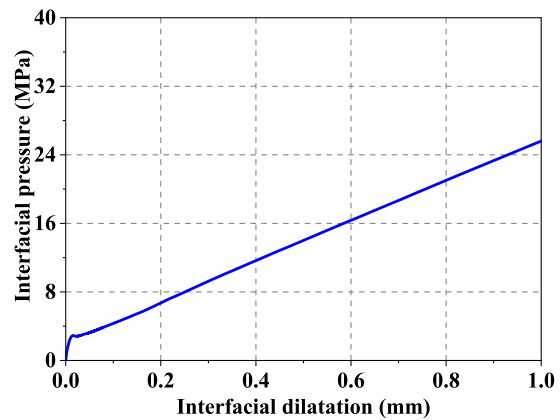
Considering the deformation of concrete is negligible, Eq. (6) can be approximated by the following equation,

$$s \approx \int \varepsilon_f dx \quad (7)$$

The slip at different locations is,



(a)



(b)

Fig. 17. Numerical results of the interfacial expansion behavior: (a) interfacial dilatation-hoop strain relationship; (b) interfacial dilatation-normal pressure relationship.

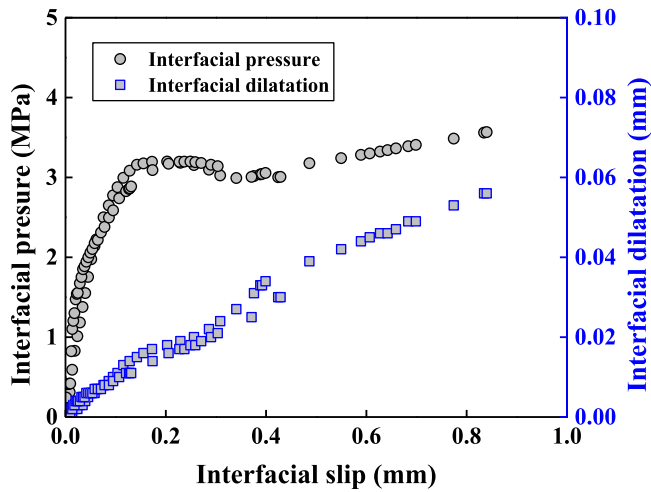


Fig. 18. Variation of interfacial dilatation and pressure with interfacial slip.

$$s_{i+1} = s_i + \Delta s_{i,i+1} \quad (8)$$

where s_{i+1} and s_i are the slips; $\Delta s_{i,i+1}$ is the difference of slip at the locations of x_{i+1} and x_i . According to Eq. (7),

$$\Delta s_{i,i+1} = \int_{x_i}^{x_{i+1}} \epsilon_f dx \quad (9)$$

Assuming a linear variation of the tensile strain ϵ_f in the very short distance $\Delta x_{i+1,i}$, Eq. (9) can be written as follows,

$$\Delta s_{i,i+1} = \frac{(\epsilon_{i+1} + \epsilon_i)}{2} \Delta x_{i+1,i} \quad (10)$$

Substituting Eq. (10) into Eq. (8),

$$s_{i+1} = \frac{(\epsilon_{i+1} + \epsilon_i)}{2} \Delta x_{i+1,i} + s_i \quad (11)$$

With the measured strains, the calculated slips at different locations can be obtained, as shown in Fig. 13(b). These slips decrease from the loaded end to the free end. By correlating the data points from Fig. 13(a) and Fig. 13(b), the bond stress-slip relationship can be obtained, as shown in Fig. 14.

4.4. Bond stress-slip relationship

The bond stress increases with the slip, and then gradually decays to zero. Overall, the bond stress-slip relationship shows a triangular shape, which is similar to the bond stress-slip relationship of dry-bonding interface with brittle failure mode [6,58–61]. Therefore, previous bond models can be adapted for the fiber-bridging interface. Numerous bond models have been proposed for FRP-concrete interface, including triangular models [59,62], parabolic models [63], exponential models [64–67], power function models [58], among others. Selecting one of the models and fitting the data points in Fig. 14 can yield a bond model for the fiber-bridging interface with brittle a failure mode. However, previous studies by Lu et al. [59], and Dai et al. [67,68] have shown that bond models based on strain gauges may exhibit significant variability due to experimental factors such as the inevitable bending of FRP plate, concrete cracks or coarse aggregates beneath the strain gauges. Therefore, an optimal method for deriving the bond models was proposed by Dai et al. [67,68]. According to Dai et al. [67,68], the loaded end-slip relationships, which can be more easily and accurately measured, are used to fit the bond model. This method is not only simple and convenient, but also avoids the drawbacks of previous approaches. Therefore, the bond model proposed by Dai et al. [67,68] is used for developing the bond model for the fiber-bridging interface.

5. Development of interfacial bond models

5.1. Bond stress-slip relationship model

According to Dai et al. [67,68], the tensile strain of FRP plate can be

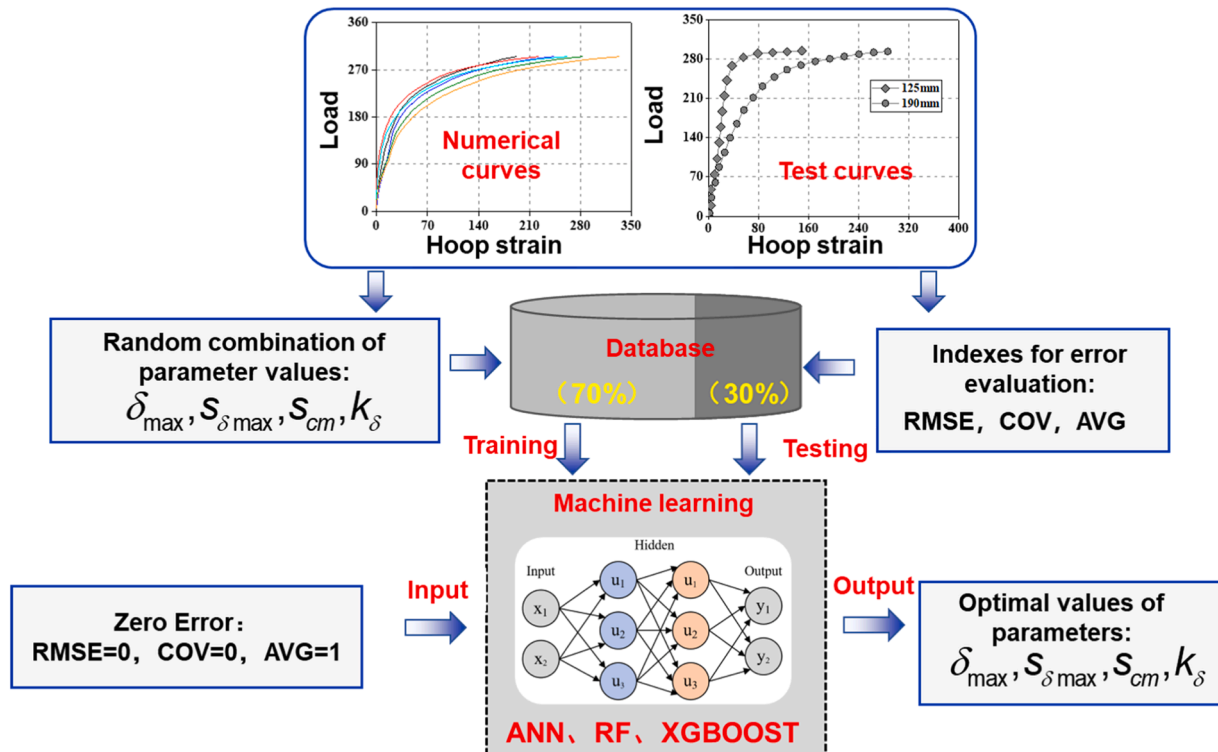


Fig. 19. The overall methodology for determining the parameters in Eq. (17).

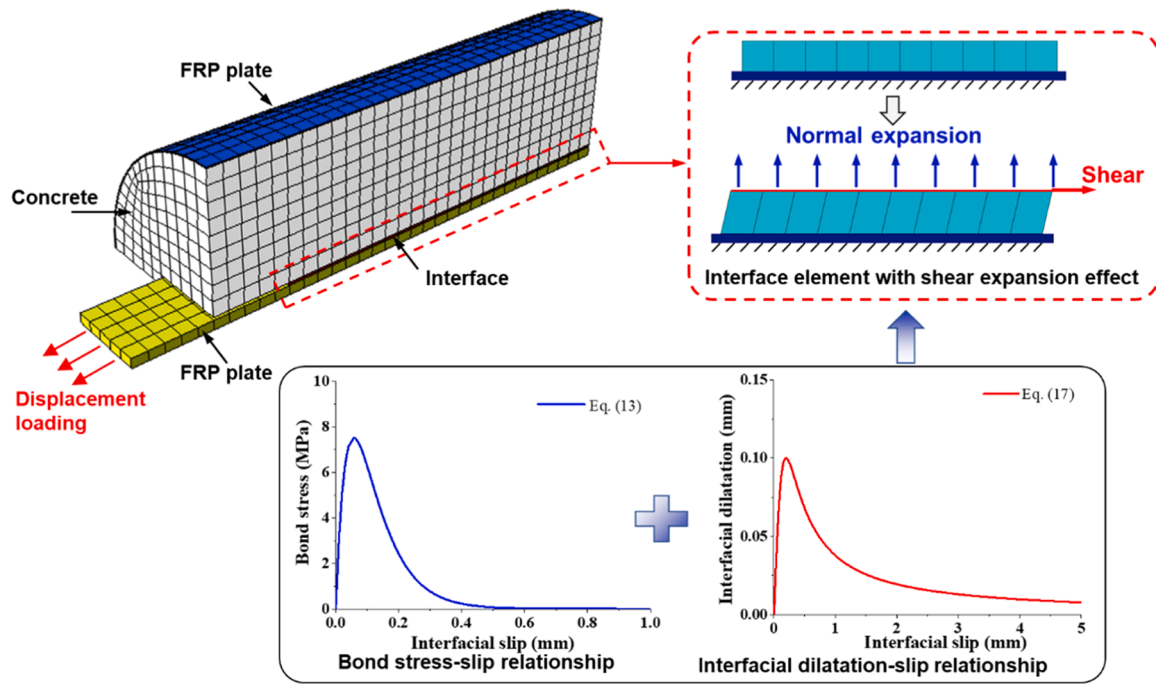


Fig. 20. FE model of pullout specimens considering shear-dilatation effects.

Table 4

Assumed values of the five parameters in Eq. (17).

Parameters	Assumed values				
δ_{max}	0.05	0.065	0.08	0.095	0.11
$s_{\delta max}$	0.8	0.95	1.1	1.25	1.4
s_{cm}	0.001	0.002	0.003	0.004	0.005
k_{δ}	1.1	1.2	1.3	1.4	1.5

approximated by the following equation,

$$\epsilon_f = A[1 - \exp(-Bs)] \quad (12)$$

where ϵ_f is tensile strain of FRP plate; s is the slip; A and B are empirical parameters.

Based on Eq. (12), the bond stress-slip relationship can be obtained as follows,

$$\tau = 2BG_f[\exp(-Bs) - \exp(-2Bs)] \quad (13)$$

$$G_f = 0.5A^2E_f t_f \quad (14)$$

where τ is the bond stress; G_f is interfacial fracture energy; t_f and E_f respectively represent the thickness and tensile modulus of the FRP plate. According to Eq. (14), when the bond length is greater than the effective bond length, the maximum load that can be reached is,

$$P_{max} = (b_f + 2\Delta b_f)(2E_f t_f G_f)^{0.5} \quad (15)$$

where b_f is the width of FRP plate; Δb_f represents the width increase considering the influence of the FRP plate width on the interfacial performance. Δb_f is 3.7 mm when $b_f \geq 100$ mm, and Δb_f is 0 when $b_f < 100$ mm [67,68].

As mentioned before, the 250 mm-long bond length has already exceeded the effective bond length. Therefore, ultimate loads of long bond length specimens (Fig. 11) can be used to determine parameter A . The average value of parameter A is 0.007. According to Eq. (12), the loaded end-slip relationship is,

$$P = A[1 - \exp(-Bs_L)]b_f t_f E_f \quad (16)$$

where s_L is the slip at the loaded end. With the tested loaded end-slip relationships in Fig. 8, the parameter B in Eq. (16) can be obtained, $B = 4.38$. With parameters A and B determined, the bond stress-slip relationship model for the fiber-bridging interface can be established. The comparison between the model prediction and the bond stress-slip data is shown in Fig. 14.

5.2. Interfacial dilatation-slip relationship model

After the initial debonding of the interface, imperfectly smooth failure surfaces are formed. When these failure surfaces continue to interact, tangential displacement induces lateral expansion, which in turn causes hoop strain in the FRP tube, as shown in Fig. 15.

To determine the interfacial expansion, a three-dimensional FE model was created to simulate the interfacial expansion behavior using ABAQUS [69]. To reduce calculation time, a quarter model was established based on symmetry conditions, as seen in Fig. 16. In this model, concrete was simulated using 8-node reduced integration solid elements (C3D8R), and the FRP tube was simulated using 4-node reduced integration shell elements (M3D4R). To ensure that the FRP tube provides strength and stiffness mainly in the circumferential direction, its Poisson's ratio was set to 0.

Based on the FE results, the variations of hoop strain of the FRP tube and interfacial pressure with interfacial dilatation were obtained, as shown in Fig. 17. Using the experimentally measured hoop strains, the interfacial dilatation and interfacial pressure can be obtained through data interpolation. These results are shown in Fig. 18. Both interfacial expansion and interfacial pressure increase with the slip. Due to the drastic failure of the interface, the attenuation of interfacial dilatation and pressure were not captured. Previous studies have shown that the interface will experience a contraction after expansion [12,21,70,71], and the interfacial expansion can be approximated by the following equation,

$$\delta = 0(0 \leq s \leq s_{cm}) \quad (17a)$$

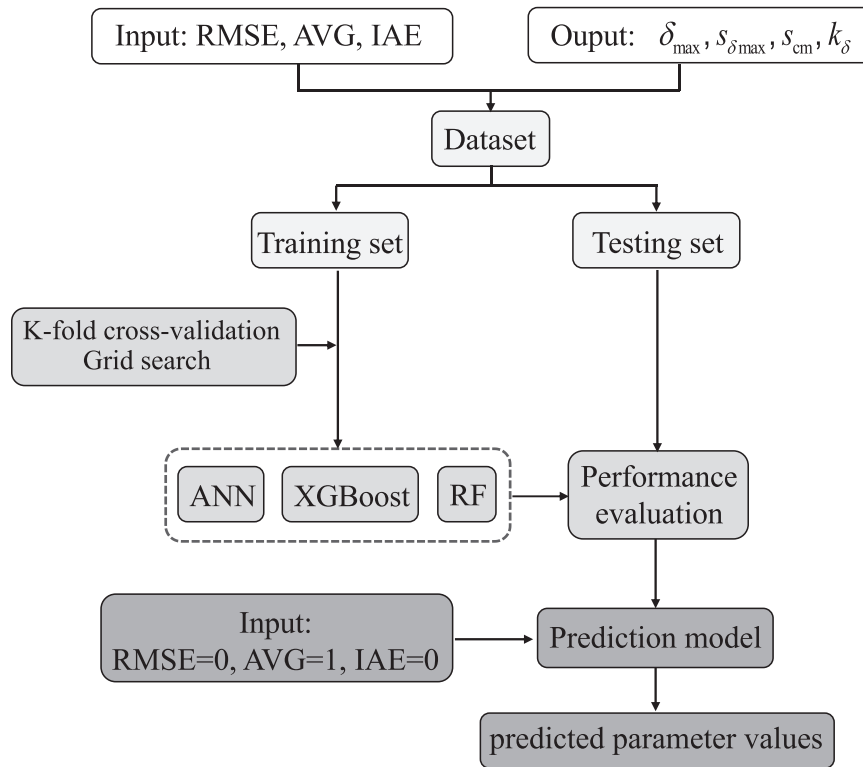


Fig. 21. Methodology of conducting the machine learning model.

$$\frac{\delta}{\delta_{\max}} = \frac{s - s_{\text{cm}}}{s_{\delta_{\max}} - s_{\text{cm}}} \frac{k_{\delta}}{k_{\delta} - 1 + \left(\frac{s - s_{\text{cm}}}{s_{\delta_{\max}} - s_{\text{cm}}}\right)^{k_{\delta}}} \quad (s_{\text{cm}} \leq s) \quad (17b)$$

where δ is the interfacial dilatation; δ_{\max} and $s_{\delta_{\max}}$ are the maximum dilatation and corresponding slip; k_{δ} is an empirical parameter; s_{cm} is the slip for initial expansion.

To determine the values of the parameters in Eq. (17), a combination of FE simulation and machine learning was employed. The overall methodology is shown in Fig. 19. First, an FE model for the specimen with a bond length of 250 mm was created. To simplify calculations, only one-fourth of the specimen was modeled based on symmetry conditions. The concrete and the FRP plate were simulated using 8-node reduced integration solid elements (C3D8R), while the FRP tube was simulated using 4-node reduced integration shell elements (M3D4R). The interface between the FRP tube and concrete was defined as hard contact in the normal direction and frictionless in the tangential direction. The ABAQUS built-in CDP model was selected as the constitutive model for concrete. The FRP plate was modeled as an anisotropic material with material properties defined using engineering constants in ABAQUS, and it was assumed not to fail. The FRP tube was modeled as an elastic material. The interaction between the FRP plate and concrete was simulated using 1 mm-thick 8-node cohesive elements (COH3D8). The tangential behavior of the interface elements was controlled by Eq. (13), while the normal behavior was controlled by Eq. (17). Fig. 20 shows the FE model.

Then the values of parameters δ_{\max} , $s_{\delta_{\max}}$, s_{cm} , and k_{δ} in Eq. (17) were randomly assumed, and a number of interfacial expansion curves were obtained. These curves were implemented into the FE model, and a number of numerical curves of load-hoop strain relationship can be obtained. The numerical curves were compared with the tested load-hoop strain curves. The deviation between numerical and tested curves were measured by three error indicators, i.e., the Root Mean Square Error (RMSE), Integral Absolute Error (IAE), and Average (AVG). In this way, a mapping relation between the values of parameters δ_{\max} ,

$s_{\delta_{\max}}$, s_{cm} , and k_{δ} and the three error indicators was established.

$$\text{RMSE} = \sqrt{\frac{1}{m} \sum_i (y_i - \hat{y}_i)^2} \quad (18a)$$

$$\text{IAE} = \sum_i \frac{\sqrt{(y_i - \hat{y}_i)^2}}{\sum_i y_i} \quad (18b)$$

$$\text{AVG} = \frac{1}{m} \sum_i \frac{y_i}{\hat{y}_i} \quad (18c)$$

$$\text{COV} = \frac{\sqrt{\sum_i \left(\frac{y_i - \text{AVG}}{y_i}\right)^2}}{\text{AVG}} \quad (18d)$$

where m is the number of samples; y_i is the true values of the data; \hat{y}_i is the estimated values of the data.

For each parameter, five possible values were assumed, see Table 4. A total of 625 curves of interfacial dilatation-slip relationship were generated. These curves were respectively input into 625 FE models to obtain the corresponding load-hoop strain response. These FE models together with the Fortran subroutines were automatically generated and submitted for analysis by a loop program in Python. The load-hoop strain curves from FE analysis were extracted by a Python program, and further discretized using MATLAB software to compare with the tested load-hoop strain curves. Thus, a database containing 625 sets of data was established with RMSE, IAE, and AVG as the output and parameters δ_{\max} , $s_{\delta_{\max}}$, s_{cm} , and k_{δ} as the input. Based on this database, three machine learning models, i.e., the BP neural network model, the random forest model, and the XGBoost model, were selected to predict the optimal parameter values [72,73].

The execution of machine learning models is illustrated in Fig. 21. First, the database was randomly divided into a training set and a testing set at a ratio of 4:1 [72,73]. Then the machine learning models were

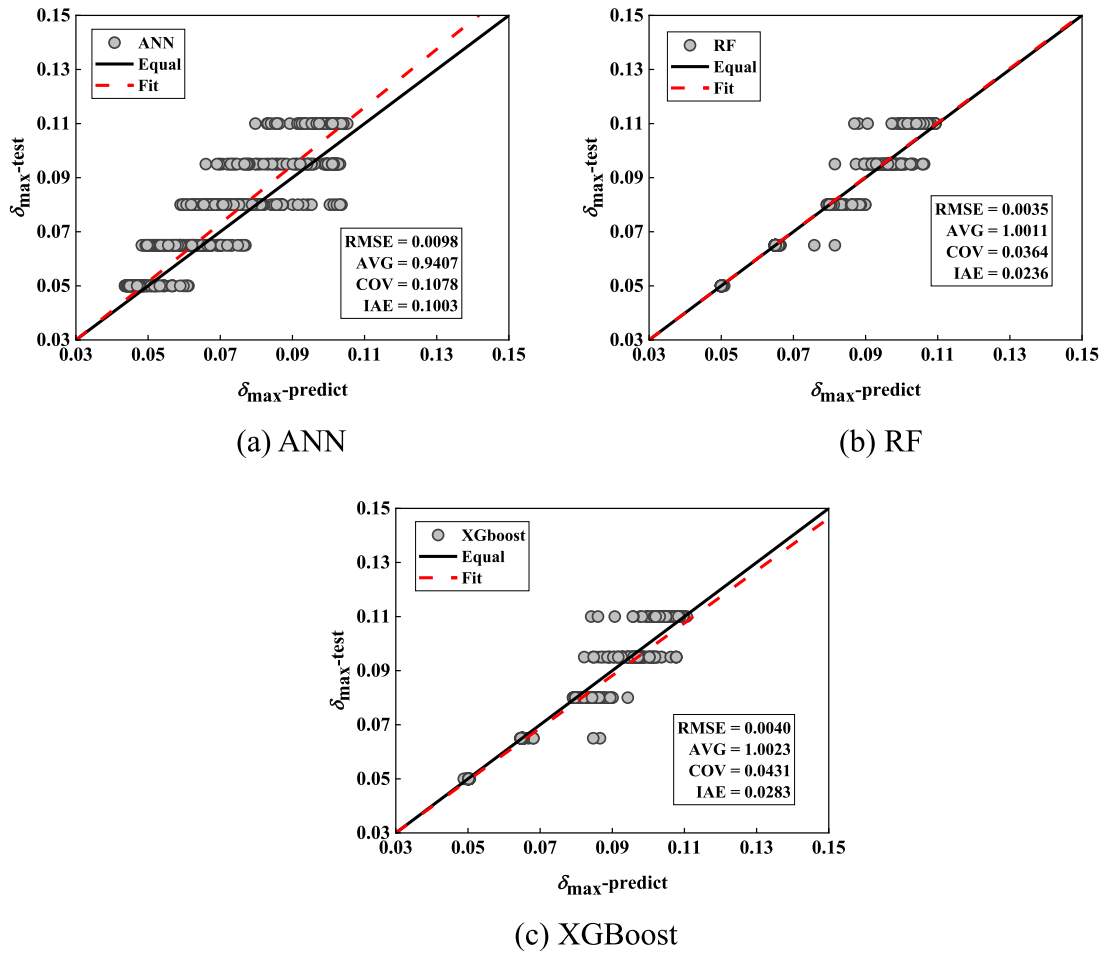


Fig. 22. Prediction performance of ANN, RF and XGBoost.

Table 5
Performance of machine learning models.

Parameters	ML model	RMSE	AVG	COV	IAE
δ_{max}	ANN	0.0098	0.9407	0.1078	0.1003
	RF	0.0035	1.0011	0.0364	0.0236
	XGBoost	0.0040	1.0023	0.0431	0.0283
$s_{\delta max}$	ANN	0.2509	1.0575	0.1941	0.1616
	RF	0.0947	1.0100	0.0899	0.0571
	XGBoost	0.1068	1.0138	0.1009	0.0698
k_s	ANN	0.1152	1.0344	0.0831	0.0724
	RF	0.0444	1.0036	0.0340	0.0228
	XGBoost	0.0527	1.0024	0.0408	0.0273
s_{cm}	ANN	0.0020	1.0506	0.8899	0.5501
	RF	0.0016	1.3572	0.6993	0.4449
	XGBoost	0.0015	1.3731	0.6462	0.4167

Table 6
Predicted values of five parameters in Eq. (17) by ML models.

ML model	Predicted values			
	δ_{max}	$s_{\delta max}$	s_{cm}	k_s
ANN	0.11	1.14	0.005	1.11
RF	0.08	1.20	0.003	1.23
XGBoost	0.10	0.85	0.006	1.11

trained using the training set, and the best hyperparameters for the models were determined through the K-fold cross-validation and grid search (K=10). The model performance was evaluated based on the

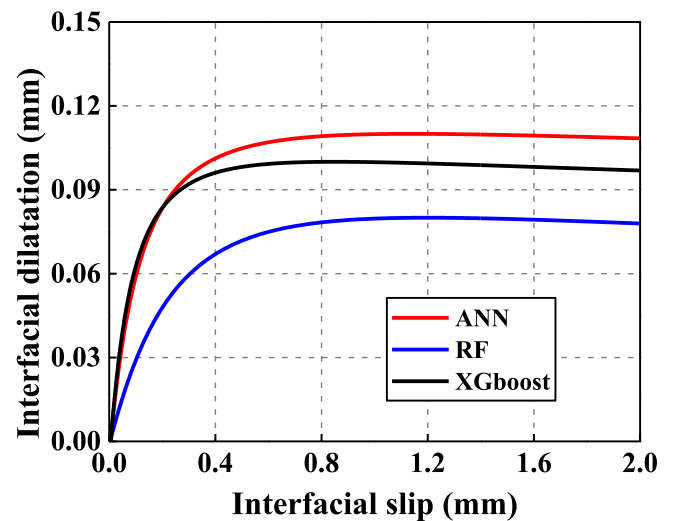


Fig. 23. Predicted interfacial dilatation-slip curve by machine learning models.

average performance, which effectively reduces the bias caused by the random sampling of the database. Grid search exhaustively combines different hyperparameter values and selects the combination that yields the best performance. Finally, the model performance was assessed using the testing set data.

All three machine learning models exhibited good performance. As an example, Fig. 22 shows comparisons between the real and predicted

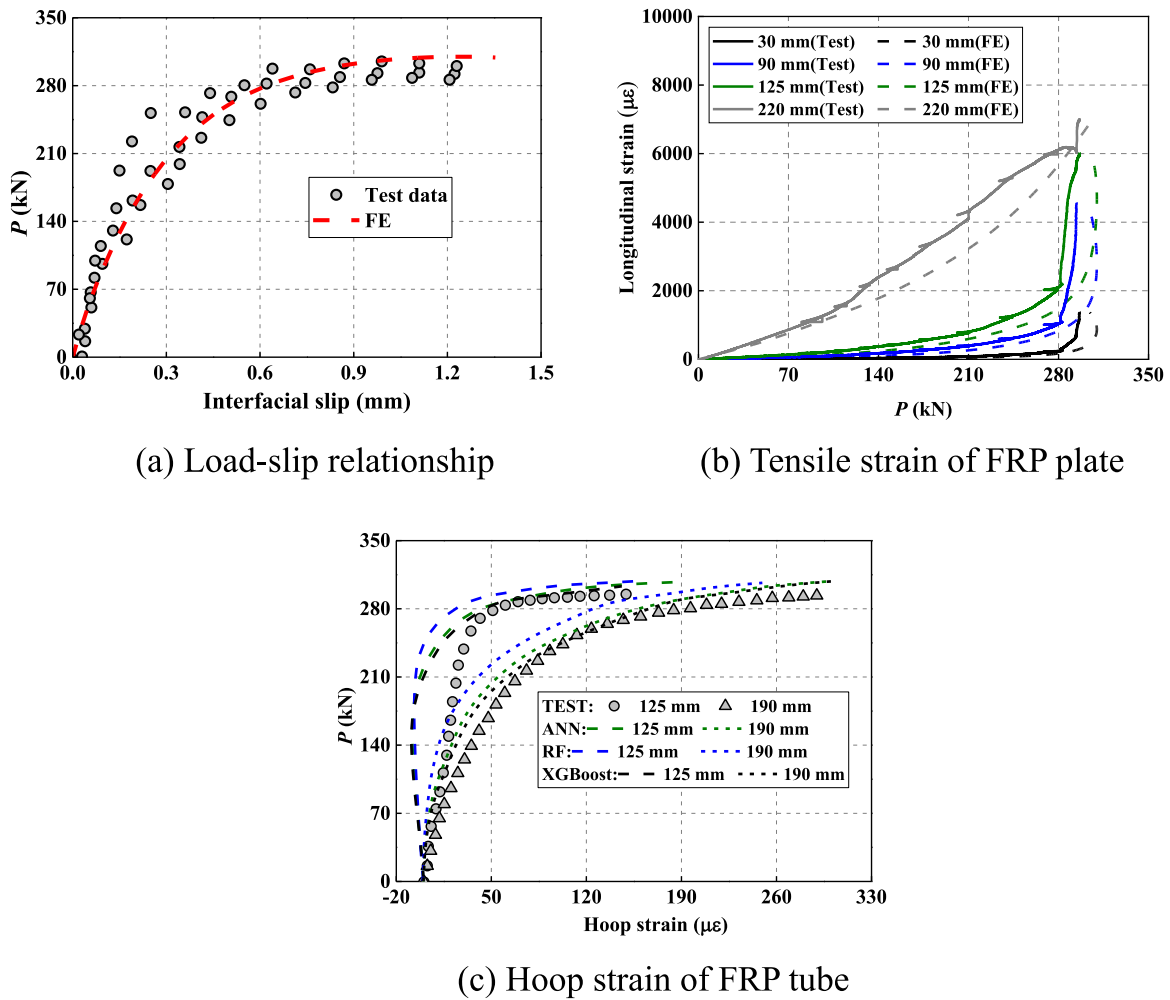


Fig. 24. Comparisons between numerical and test results of specimen L-V1-1.

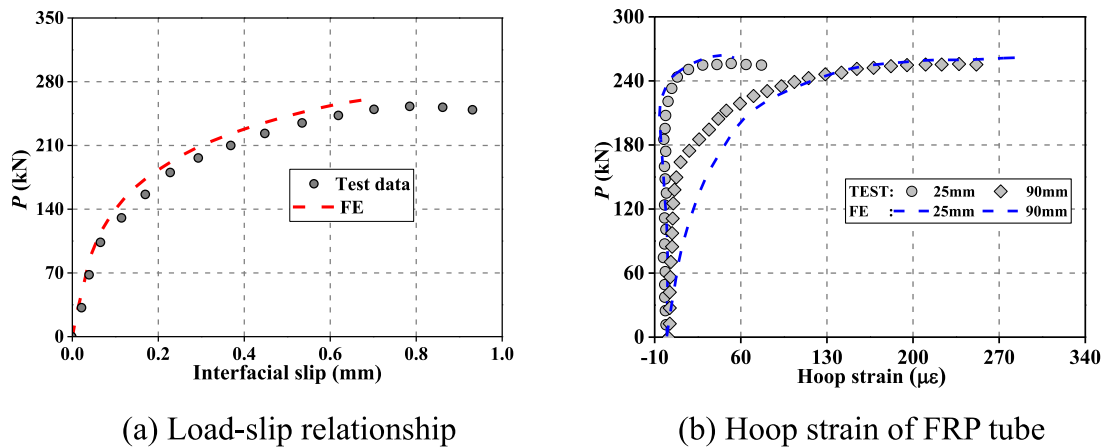


Fig. 25. Comparisons between numerical and test results of short bond-length specimen S-V1-3.

values of parameter δ_{max} . The predicted values of δ_{max} were very close to the real values. To assess the model performance more intuitively, four error indicators for the three machine learning models were calculated, i.e., the Root Mean Square Error (RMSE, Eq. 18a), the Average (AVG, Eq. 18b), the Coefficient of Variation (COV, Eq. 18c), and the Integrated Absolute Error (IAE, Eq. 18d), as shown in Table 5. It is evident that all three machine learning models provided relatively good predictions.

After model training and validation of model accuracy, the optimal

values of parameters δ_{max} , $s_{\delta_{max}}$, s_{cm} , and k_{δ} , could be obtained by setting $RMSE=0$, $IAE=0$, $AVG=1$. The results are shown in Table 6, and the corresponding interfacial dilatation-slip relationship curves are shown in Fig. 23. As can be seen, the predicted values of these parameters are very close.

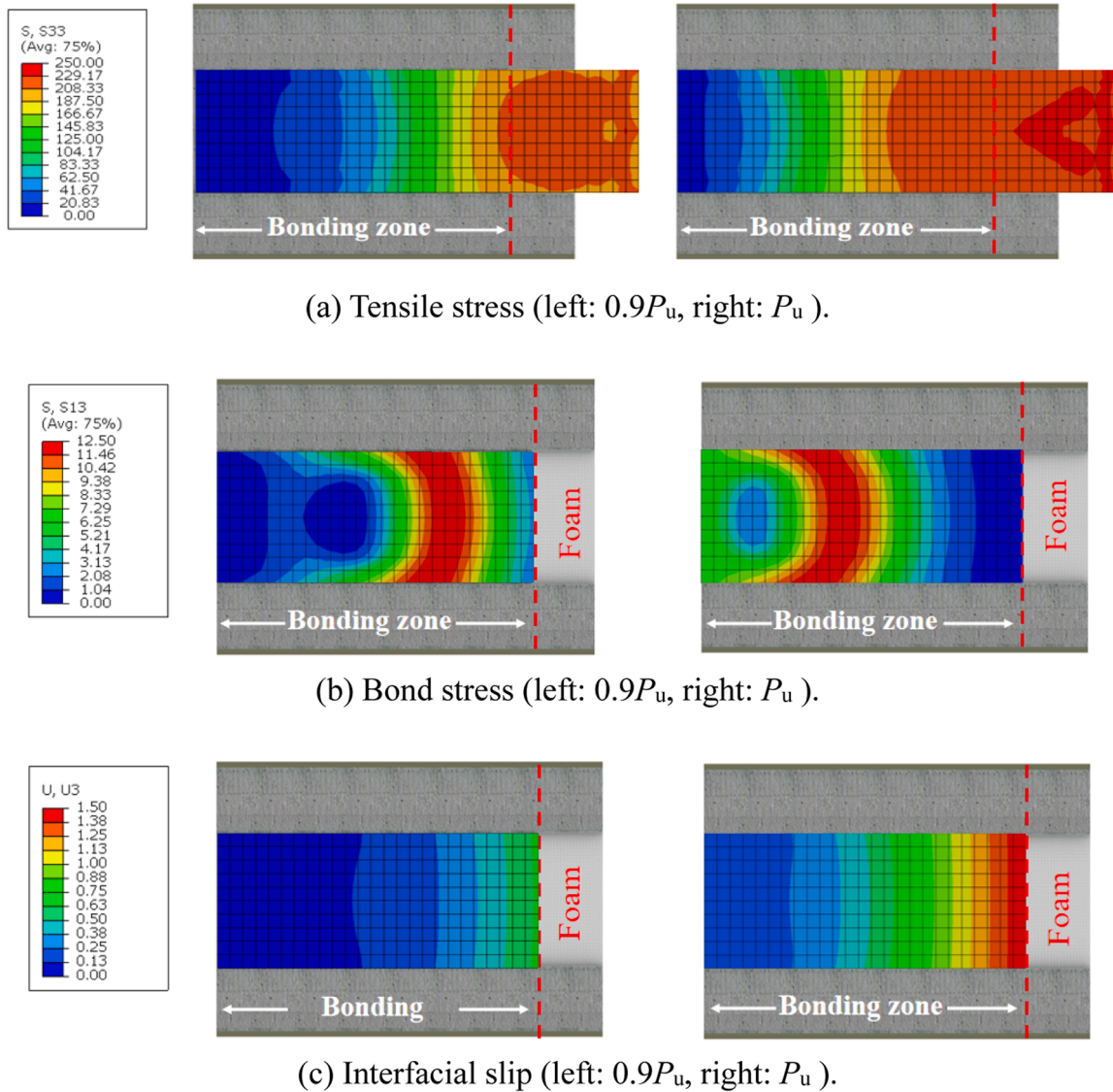


Fig. 26. Interfacial state at the load of $0.9P_u$ and peak load.

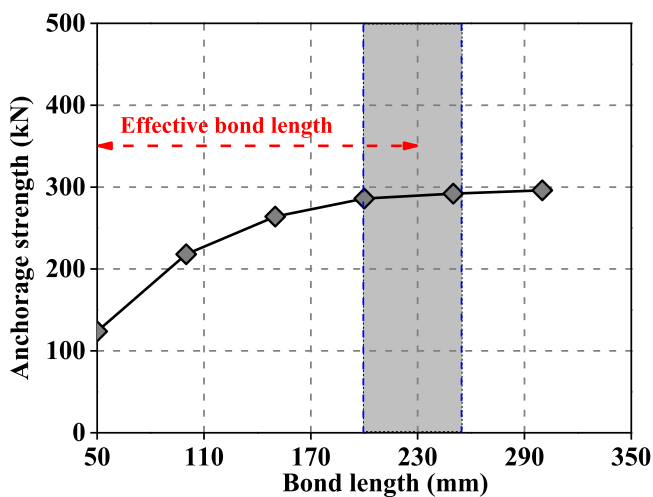


Fig. 27. Variation of anchorage strength with bond length.

5.3. Verification of the proposed models

Equation (13) and Eq. (17) respectively govern the tangential and normal behavior of the fiber-bridging interface. To validate the effectiveness of the proposed interfacial models, the tests results were simulated based on the FE model introduced in Section 5.2. Fig. 24 and Fig. 25 show the comparisons between numerical and experimental results.

It can be observed that the load-slip relationships can be well predicted by FE models. The tensile strain of the FRP plate at different locations also matches very well with the experimental results. This indicates that the proposed bond stress-slip relationship model, i.e., Eq. (13), is reasonable. Comparisons in Fig. 24(c) and Fig. 25(b) reveal that the numerical results based on three machine learning algorithms are relatively close. In comparison with the hoop strain at the 190 mm position, the hoop strain at a height of 125 mm is not well predicted in the initial stage for the specimen L-V1-1. This is because the interfacial expansion develops from the loaded end to the free end, which will cause bending of the FRP tube in the longitudinal direction and consequently hoop compression. The slight compression of FRP tube in the hoop direction was not well captured during the loading of specimen L-V1-1, however, this phenomenon is more noticeable in the specimen S-

V1–3 (Fig. 25b).

Fig. 26 illustrates the state of the interface at $0.9 P_u$ and P_u . The tensile stress of the FRP plate generally decreases from the loaded end to the free end. At the loaded end, there exists a zone where the stress gradient is close to 0 and this zone propagates towards the free end. This phenomenon is consistent with the test results presented in Section 3.2. In Fig. 26(b), the peak of bond stress shifts towards the free end. At P_u , the bond stress is only distributed in a certain region which corresponds to the effective bond length. Fig. 26(c) represents the slip at different locations. The slip reduces from the loaded end to the free end. At the peak load, the region near the free end has not been fully activated, resulting in very small slip.

To further analyze the mechanical performance of the fiber-bridging interface, parameter analysis was conducted based on the FE model described above. FE models with different bond lengths were created, and the anchorage strength or the ultimate loading capacity was calculated. Fig. 27 shows the variation of the numerical anchorage strength with bond length. The anchorage strength increases with the bond length in a decaying slope, and almost plateaus when the bond length reaches around 200 mm. This indicates that the effective bond length is around 200 mm.

6. Conclusion

Based on the experimental and numerical results, as well as discussions above, the following conclusions can be drawn:

- (1) With a high fiber volume fraction (1.5 % and 3.0 %), the fiber-bridging interface exhibits brittle failure at the surface of the FRP plate. Under this failure mode, the interfacial behavior is governed by the bond between the prefabricated fiber-bridging slab and the FRP plate.
- (2) The bond stress-slip relationships of the fiber-bridging interface with brittle failure mode is established using the measured strains of the FRP plate. Based on a well-known FRP-concrete interface model in the literature, a bond stress-slip model is established using the load-loaded end slip curves, and the model agrees well with the tested bond stress-slip relationships.
- (3) A combined approach of finite element simulation and machine learning prediction is employed to determine the normal expansion behavior of the fiber-bridging interface with brittle failure mode. The three machine learning models, i.e., the BP neural network model, the random forest model, and the XGBoost model all can provide reasonable predictions.
- (4) A comprehensive FE model is developed based on the bond stress-slip relationship and expansion-slip relationships. This FE model accurately simulates both the tangential and normal behavior of the fiber-bridging interface with brittle failure mode. Simulation results confirm the validity of these models.
- (5) The effective bond length of the fiber-bridging interface under brittle failure mode is approximately 200 mm. Beyond this length, further increasing the bond length does not enhance anchorage strength.

CRedit authorship contribution statement

Hongwei Lin: Writing – original draft, Investigation, Funding acquisition, Conceptualization. **Peng Feng:** Supervision, Methodology, Conceptualization. **Haidong Qu:** Writing – review & editing, Investigation, Formal analysis. **Guanzhi Cheng:** Validation, Resources, Funding acquisition. **Huixin Zeng:** Writing – original draft, Investigation, Formal analysis.

Declaration of Competing Interest

The authors declare that they have no known competing financial

interests or personal relationships that could have appeared to influence the work reported in this paper.

Acknowledgements

This work was supported by the National Natural Science Foundation of China (Nos. 52108109, 52478118), the Talent Fund of Beijing Jiaotong University (No. 2021RC232), the Open Research Fund by the Key Laboratory of Concrete and Pre-stressed Concrete Structure of Ministry of Education (CPCSME2018-02), and the Research Programs of CARS (No. 2022YJ091).

Data Availability

Data will be made available on request.

References

- [1] Hou B, Li X, Ma X, Du C, Zhang D, Zheng M, et al. The cost of corrosion in China. *npj Mat Degrad* 2017;1:4.
- [2] Liu T, Liu X, Feng P. A comprehensive review on mechanical properties of pultruded FRP composites subjected to long-term environmental effects. *Compos Part B Eng* 2020;191:107958.
- [3] Liu T, Feng P, Tang J, Liu X. Pullwinding technique for realizing hybrid roving architecture in pultruded GFRP composites. *Compos Struct* 2023;305:116483.
- [4] Liu T, Wang R, Zhen S, Feng P. A binary resin system of epoxy and phenol-formaldehyde for improving the thermo-mechanical behavior of FRP composites. *Constr Build Mater* 2023;389:131790.
- [5] Teng J. New-material hybrid structures. *China Civ Eng J* 2018;51:1–11.
- [6] Zhang P, Wu G, Zhu H, Meng S, Wu Z. Mechanical performance of the wet-bond interface between FRP plates and cast-in-place concrete. *J Compos Constr* 2014;18:04014016.
- [7] Zhang P, Zhu H, Wu G, Meng S, Wu Z. Shear capacity comparison of four different composite interfaces between FRP plates and concrete substrate. *J Compos Constr* 2016:04016006.
- [8] Zhang L, Wang W, Harries K, Tian J. Bonding behavior of wet-bonded GFRP-concrete interface. *J Compos Constr* 2015;19:04015001.
- [9] Li L, Shao Y, Wu Z. Durability of wet bond of hybrid laminates to cast-in-place concrete. *J Compos Constr* 2010;14:209–16.
- [10] Shao Y, Wu Z, Bian J. Wet-bonding between FRP laminates and cast-in-place concrete. International symposium on bond behaviour of FRP in structures, IIFC, Hong Kong, 2005.
- [11] Wang W, Huang H, Zhao F. Experimental study on bonding behavior of GFRP plate and concrete interface based on wet bonding technique. *China Civ Eng J* 2015;48:52–60.
- [12] Lin H, Zeng H, Feng P, Jiang C, Zhang Y. Bond behavior of FRP-concrete wet-bonding interface under lateral confinement. *Eng Struct* 2023;292:116536.
- [13] Guo S, Kong B, Cai C, Zhang J, Zeng X. Experimental study on the interface behavior of GFRP-concrete composite deck. *Eng Mech* 2017;34:216–25.
- [14] Cho K, Park S, Kim S, Cho J, Kim B. Freeze-thaw effect on coarse sand coated interface between FRP and concrete. *Eng* 2013;5:807–15.
- [15] Yuan J, Hadi M. Bond-slip behaviour between GFRP I-section and concrete. *Compos Part B Eng* 2017;130:76–89.
- [16] Cho K, Cho J, Chin W, Kim B. Bond-slip model for coarse sand coated interface between FRP and concrete from optimization technique. *Compos Struct* 2006;84:439–49.
- [17] Cho J, Cho K, Park S, Kim S, Kim B. Bond characteristics of coarse sand coated interface between stay-in-place fibre-reinforced polymer formwork and concrete based on shear and tension tests. *Can J Civ Eng* 2010;37:706–18.
- [18] Goyal R, Mukherjee A, Goyal S. An investigation on bond between FRP stay-in-place formwork and concrete. *Constr Build Mater* 2016;113:741–51.
- [19] Wang Y, Hao Q, Ou J. Experimental investigation on bond behavior for coarse sand coated interface between FRP plate and concrete. *J Wuhan Univ Technol* 2007;31:393–6.
- [20] Oliva M., Bank L., Bae H., Barker J., Yoo S. FRP stay-in-place formwork and reinforcing for concrete highway bridge decks. In: Proceedings of FRPRCS 8, 8th international symposium on FRP in reinforced concrete structures, Patras, Greece; 2007.
- [21] Lin H, Feng P, Yang J. Pressure-dependent bond stress-slip model for sand-coated FRP-concrete interface. *Compos Struct* 2021;263:113719.
- [22] Zou X, Feng P, Wang J. Bolted shear connection of FRP-concrete hybrid beams. *J Compos Constr* 2018;22:04018012.
- [23] Zou X, Feng P, Bao Y, Wang J, Xin H. Experimental and analytical studies on shear behaviors of FRP-concrete composite sections. *Eng Struct* 2020;215:110649.
- [24] Zou X, Feng P, Wang J, Wu Y, Feng Y. FRP stay-in-place form and shear key connection for FRP-concrete hybrid beams/decks. *Compos Struct* 2018;192:489–99.
- [25] Zou X, Feng P, Wang J. Perforated FRP ribs for shear connecting of FRP-concrete hybrid beams/decks. *Compos Struct* 2016;152:267–76.
- [26] Nguyen H, Mutsuyoshi H, Zatar W. Push-out tests for shear connections between UHPFRC slabs and FRP girder. *Compos Struct* 2014;118:528–47.

- [27] Xue W, Yan D, Zhang S. Push-out behavior of GFRP bolts shear connectors in FRP-concrete hybrid beam. *Eng Struct* 2023;294:116758.
- [28] Etim O, Gand A, Saidani M, Fom P, Ganjian E, Okon E. Shear characterisation of pultruded superstructural FRP-concrete push-outs. *Structures* 2020;23:254–66.
- [29] Rajchel M, Kulpa M, Siwowski T. Experimental study on a novel shear connection system for FRP-concrete hybrid bridge girder. *MDPI Mater* 2020;13:2045.
- [30] Honickman H, Nelson M, Fam A. Investigation into the bond of glass fiber-reinforced polymer stay-in-place structural forms to concrete for decking applications. *Transp Res Rec* 2009;2131:134–44.
- [31] Correia J, Branco F, Ferreira J. GFRP-concrete hybrid cross-sections for floors of buildings. *Eng Struct* 2009;31:1331–43.
- [32] Nordin H, Täljsten B. Testing of hybrid FRP composite beams in bending. *Compos Part B Eng* 2004;35:27–33.
- [33] Honickman H, Fam A. Investigating a structural form system for concrete girders using commercially available GFRP sheet-pile sections. *J Compos Constr* 2009;13:455–65.
- [34] Feng P, Lu X, Ye L. Application of fiber reinforced polymer in construction: experiment, theory and methodology. Beijing, China: China Architecture & Building Press.; 2011.
- [35] Nguyen H, Mutsuyoshi H, Zatar W. Hybrid FRP-UHPFRC composite girders: Part 1—Experimental and numerical approach. *Compos Struct* 2015;125:631–52.
- [36] Canning L, Hollaway L, Thorne A. An investigation of the composite action of an FRP/concrete prismatic beam. *Constr Build Mater* 1999;13:417–26.
- [37] Gai X, Darby A, Ibell T, Evernden M. Experimental investigation into a ductile FRP stay-in-place formwork system for concrete slabs. *Constr Build Mater* 2013;49:1013–23.
- [38] Ogueji EC, Hosain MU. A parametric study of perfbond rib shear connectors. *Can J Civ Eng* 1994;21614–25.
- [39] Zellner W. Recent designs of composite bridges and a new type of shear connectors. *Compos Constr Steel Concr* 1988.
- [40] Cho K, Park S, Kim S, Cho J, Kim B. Shear connection system and performance evaluation of FRP-concrete composite deck. *KSCE J Civ Eng* 2010;14:855–65.
- [41] Lameiras R, Barros J, Valente I, Xavier J, Azenha M. Pull-out behaviour of glass-fibre reinforced polymer perforated plate connectors embedded in concrete. Part II: prediction of load carrying capacity. *Constr Build Mater* 2018;169:142–64.
- [42] Liu Y., He J., Fan H., Chen A., Dai L. Experimental study on flexural behaviour of hybrid GFRP/concrete bridge deck. Proceedings of the 5th international conference on FRP composites in civil engineering (CICE 2010), 2010, Beijing, China.
- [43] Xue W., Ge C., Tan Y., Wang Y. Experimental studies on FRP-concrete composite deck with FRP perfbond shear connectors. Advances in FRP Composites in Civil Engineering: Proceedings of the 5th International Conference on FRP Composites in Civil Engineering (CICE 2010), 2010, Beijing, China.
- [44] Nam J, Yoon S, Ok D, Cho S. Perforated FRP shear connector for the FRP-concrete composite bridge deck. *Key Eng Mater: Trans Tech Publ* 2007;334:381–4.
- [45] Zuo Y, Mosallam A, Xin H, Liu Y, He J. Flexural performance of a hybrid GFRP-concrete bridge deck with composite T-shaped perforated rib connectors. *Compos Struct* 2018;194:263–78.
- [46] Zuo Y, Liu Y, He J. Experimental investigation on hybrid GFRP-concrete decks with T-shaped perforated ribs subjected to negative moment. *Constr Build Mater* 2018;158:728–41.
- [47] Xue W, Zhang S, Ge C. Experimental study on the shear connectors of FRP-concrete hybrid beam. *J Highw Transp Res Dev* 2014;1:207–10.
- [48] Zhang P, Liu H, Gao D, Zhao J, Feng H, Tang G. Shear-bond behavior of the interface between FRP profiles and concrete by the double-lap push shear method. *J Compos Constr* 2017;21:4017012.
- [49] Feng P, Li Z, Wang J, Liu T. Novel joint for pultruded FRP beams and concrete-filled FRP columns: conceptual and experimental investigations. *Compos Struct* 2022;287:115339.
- [50] Li G, Yang Y, Yang Z, Fang C, Ge H, Liu Y. Mechanical behavior of high-strength concrete filled high-strength steel tubular stub columns stiffened with encased I-shaped CFRP profile under axial compression. *Compos Struct* 2021;275:114504.
- [51] Hadi M, Yuan J. Experimental investigation of composite beams reinforced with GFRP I-beam and steel bars. *Constr Build Mater* 2017;144:462–74.
- [52] De Borst R, Crisfield M, Remmers J, Verhoosel C. Nonlinear finite element analysis of solids and structures. John Wiley & Sons.; 2012.
- [53] Liu K, Wu Y. Analytical identification of bond-slip relationship of EB-FRP joints. *Compos Part B Eng* 2012;43:1955–63.
- [54] Wu Y, Xu X, Sun J, Jiang C. Analytical solution for the bond strength of externally bonded reinforcement. *Compos Struct* 2012;94:3232–9.
- [55] Yuan H, Teng J, Seracino R, Wu Z, Yao J. Full-range behavior of FRP-to-concrete bonded joints. *Eng Struct* 2004;26:553–65.
- [56] Wu Z, Yuan H, Niu H. Stress transfer and fracture propagation in different kinds of adhesive joints. *J Eng Mech* 2002;128:562–73.
- [57] Chen J, Teng J. Anchorage strength models for FRP and steel plates bonded to concrete. *J Struct Eng* 2001;127:784–91.
- [58] Nakaba K, Kanakubo T, Furuta T, Yoshizawa H. Bond behavior between fiber-reinforced polymer laminates and concrete. *Acids Struct J* 2001;98:359–67.
- [59] Lu X, Teng J, Ye L, Jiang J. Bond-slip models for FRP sheets/plates bonded to concrete. *Eng Struct* 2005;27:920–37.
- [60] Ferracuti B, Savoia M, Mazzotti C. Interface law for FRP-concrete delamination. *Compos Struct* 2007;80:523–31.
- [61] Lu X, Ye L, Teng J, Jiang J. Meso-scale finite element model for FRP sheets/plates bonded to concrete. *Eng Struct* 2005;27:564–75.
- [62] Monti M, Renzelli M, Luciani P. FRP adhesion in uncracked and cracked concrete zones. Proc of 6th international symposium on FRP reinforcement for concrete structures. Singapore: World Scientific Publications.; 2003. p. 183–92.
- [63] Biscaia H, Chastre C, Silva M. Linear and nonlinear analysis of bond-slip models for interfaces between FRP composites and concrete. *Compos Part B Eng* 2013;45:1554–68.
- [64] Dai J., Ueda T. A nonlinear bond stress-slip relationship for FRP sheet-concrete interface. The international symposium on latest achievement of technology and research on retrofitting concrete structures: Japan Concrete Institute; 2003. 107–12.
- [65] Savoia M, Ferracuti B, Mazzotti C. Non linear bond-slip law for FRP-concrete interface. fibre-reinforced polymer reinforcement for concrete structures. World Scientific Publications.; 2003. p. 163–72.
- [66] Yuan H, Wu Z, Yoshizawa H. Theoretical solutions on interfacial stress transfer of externally bonded steel/composite laminates. *J Struct Mech Earthq Eng JSCE* 2001;18:27–39.
- [67] Dai J, Ueda T, Sato Y. Development of the nonlinear bond stress-slip model of fiber reinforced plastics sheet-concrete interfaces with a simple method. *J Compos Constr* 2005;9:52–62.
- [68] Dai J, Ueda T, Sato Y. Unified analytical approaches for determining shear bond characteristics of FRP-concrete interfaces through pullout tests. *J Adv Concr Technol* 2006;4:133–45.
- [69] Abaqus. ABAQUS Analysis User's Manual. Version 2013;6:13.
- [70] Lin H, Song Z. Bond model for deformed steel bar under lateral confinement. Technical report. Beijing, China: Beijing Jiaotong University.; 2023.
- [71] Bamonte P, Gambarova P. High-bond bars in NSC and HPC: Study on size effect and on the local bond stress-slip law. *J Struct Eng* 2007;133:225–34.
- [72] Liu X, Liu T, Feng P. Long-term performance prediction framework based on XGBoost decision tree for pultruded FRP composites exposed to water, humidity and alkaline solution. *Compos Struct* 2022;284:115184.
- [73] Liu X. Study on Long-Term Performance and Prediction of Pultruded FRP in Marine Environment. Tsinghua University.; 2021.